Crustal and upper mantle structure across the Dead Sea rift and Israel from teleseismic P-wave tomography and gravity data

A. Hofstetter[a,*], C. Dorbath[b], M. Rybakov[a], V. Goldshmidt[a]

[a]Geophysical Institute of Israel, P.O. Box 182, Lod 71100, Israel
[b]IRD and Institut de Physique du Globe, 5 rue Rene Descartes, 67084 Strasbourg Cedex, France

Abstract

New findings of the structure of the crust and the upper mantle across the Dead Sea rift and Israel were obtained by applying P and PKP wave relative travel time residuals inversion of 612 teleseisms, recorded by the seismic networks in Israel and Jordan. Independently of the relative teleseismic travel time residuals, the Bouguer gravity anomalies were used as an additional aid to examine the structure of the crust and upper mantle. An examination of the teleseismic travel time residuals in Israel suggests the existence of two prominent provinces of distinct crustal structure. The northward increase of the teleseismic travel time residuals is in good agreement with a gradual thickening of the sedimentary sequence and a simultaneous thinning of the crust. Examination of the inverted velocity anomalies indicates that the upper and lower crusts are sub-divided into a number of structures. We identify several velocity anomalies that are associated with prominent geological structures. The southern Dead Sea basin is characterized with the largest decrease of velocity, in both upper and lower crustal layers, due to the infilling of light material relative to the surrounding material. The velocity anomaly in the Carmel structure is probably associated with variations in the upper part of the upper mantle. Examination of a cross-section that traverses the Dead Sea transform supports the existence of lighter mass density material on the eastern side relative to that on the western side. © 2000 Elsevier Science B.V. All rights reserved.

Keywords: tomography; gravity; Dead Sea; teleseisms

1. Introduction

Seismic refraction studies of the crust of Israel and Jordan (Ginzburg et al., 1979a,b; Ginzburg and Folkman, 1980; Makris et al., 1983; El-Isa et al., 1987) reveal that Israel is a transition zone between the continental crust of the Arabian Shield and the oceanic crust of the Eastern Mediterranean Sea. Close to the Arabian Shield the crustal thickness is about 32–37 km, and a relatively thin sequence of sediments is observed, while the oceanic crust has a thick sedimentary sequence, and the total crustal thickness is about 20 km. Recent findings of seismic refraction data and geological evidence (Ben-Avraham and Ginzburg, 1990), as well as Bouguer gravity (Ten Brink et al., 1990; Hofstetter et al., 1991) and teleseismic P-wave travel time residual anomalies (Hofstetter et al., 1991) questioned several inconsistencies of the former crustal model. In general, these findings suggest a model in which a significant northward stepwise thickening of the sedimentary wedge, away from the Arabian Shield and towards the Eastern Mediterranean region occurs. Consequently, based on these studies, it

* Corresponding author.
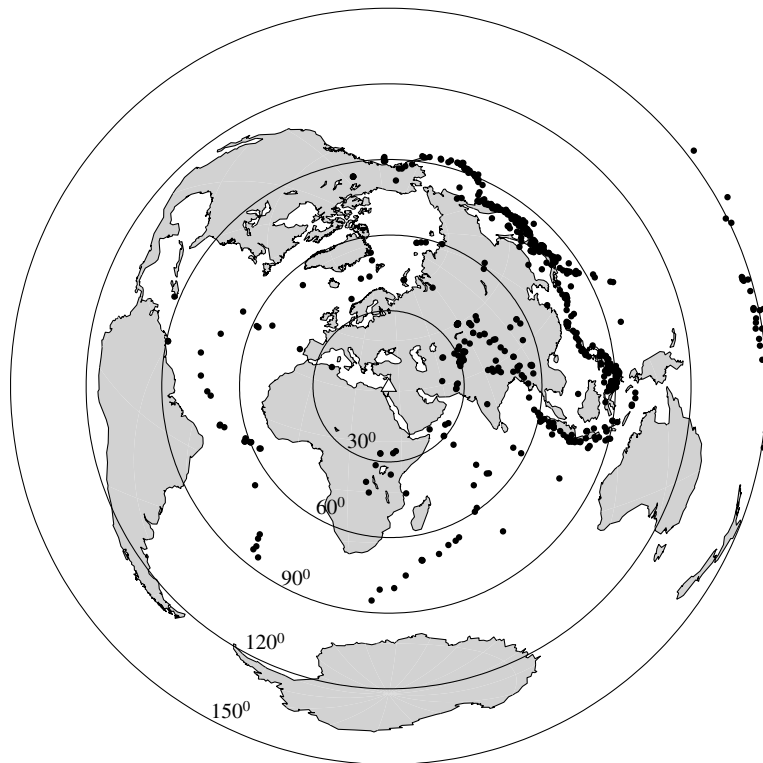 E-mail address: rami@iprg.energy.gov.il (A. Hofstetter).

Fig. 1. Distribution of event locations (solid circles) that were used in this study, centered in BGIO (triangle).

appears that the crustal model of the northern part of this shield should be revised. Moreover, since none of those studies obtained an accurate model of the crust and the upper part of the upper mantle, we here utilize the method of teleseismic tomography for obtaining a deeper insight of the structure of this region.

Teleseismic P-wave residuals inversion can serve as an effective tool for studying the seismic properties of the crust and upper mantle (e.g. Ellsworth and Koyanagi, 1977; Achauer, 1992; Engdahl et al., 1995; Dorbath et al., 1996; Wittlinger et al., 1998). The new contribution of this study is the better understanding of the structure of the crust and the upper mantle, via the analysis of teleseismic data, recorded by the Israeli seismic network and several Jordanian stations located on the eastern side of the Dead Sea transform (DST), observed for over a decade (1984–1994). In this study, we focus on the changes of the velocity structure of the DST region, and on the velocity variations of the crustal and upper mantle that underlies Israel and the eastern Mediterranean Sea.

To afford additional constraint, we verify the consistency between velocity changes, borehole sections, Bouguer gravity anomalies and magnetic anomalies.

2. Method of analysis and teleseismic data reduction

2.1. Teleseismic data reduction

A compilation of 612 teleseismic events, at epicentral distances between 20 and 150°, during March 1984 to April 1994 was used (Fig. 1). The source parameters of these events are determined by the National Earthquake Information Service (NEIS). Most of the events occurred at typical distances of 60–90°. A total of about 12,000 P-wave arrivals are read from the recording of the short-period vertical component seismic stations (Fig. 2 and Table 1), reported by the Israel Seismic Network Bulletins (1984–1994) and the Jordan Seismic Observatory
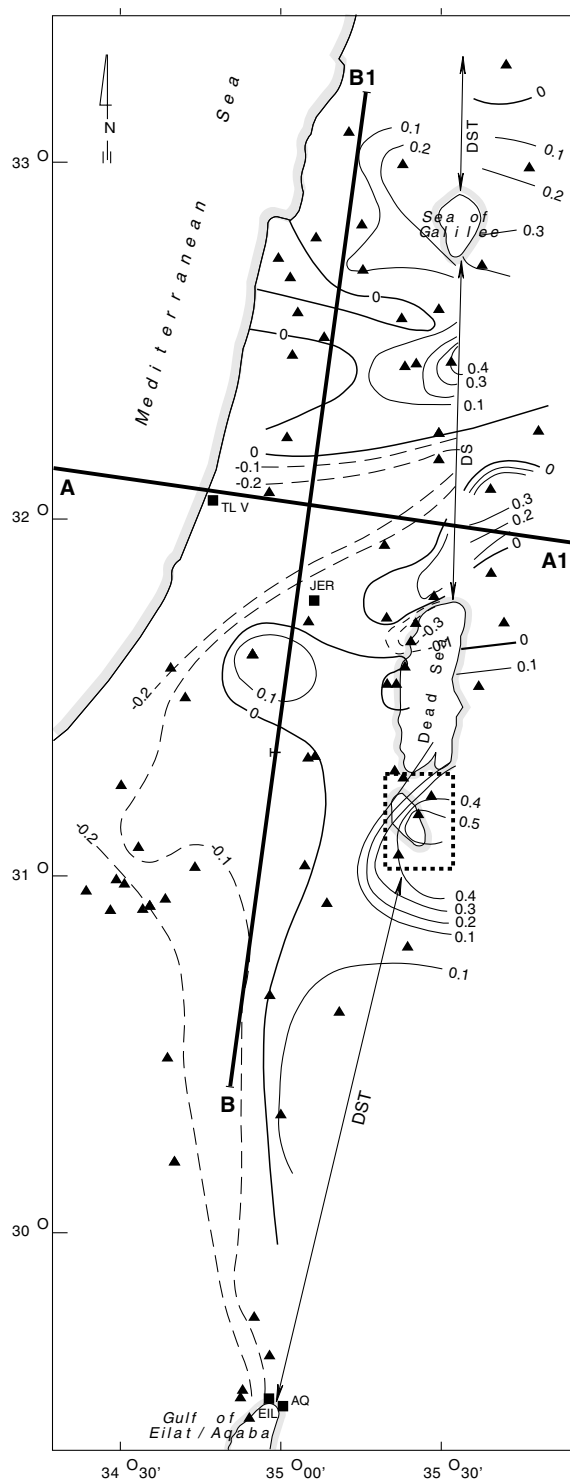
Bulletins (1984–1994). Hereafter the combined network is called the Dead Sea Regional Network (DSRN). There is an abundant number of strong earthquakes from the northeast quadrant (mainly western Pacific Ocean and eastern Asia), versus a relatively small number of strong earthquakes from other quadrants (i.e. Atlantic Ocean), resulting in an unequal azimuthal coverage of teleseismic events (Fig. 1). All traces of each event were visually compared and correlated using distinct phases such as P or PKP, and prominent phases as pP or pPKP immediately following the first onset. The reading error is estimated to be less than 0.05 s. We discarded doubtful readings, i.e. unclear arrivals or poor signal to noise ratio. Because of the relatively small size of the network, systematic errors, caused by event mislocation, and variation of the ray path shapes to the seismic stations, are estimated to be less than 0.05 s (Engdahl et al., 1977). A velocity of 4.0 km/s, based on crustal refraction studies (Ginzburg et al., 1979a,b; Ginzburg and Folkman, 1980), was applied for an elevation correction to the mean sea level.

In order to minimize the source effect resulting from incorrect hypocenter location and origin time, and to minimize effects due to inhomogeneities along the ray paths, away from the study area, we use travel time residuals. The raw teleseismic travel time residuals are given by $t_{ij} = T_{ij}(\text{obs}) - T_{ij}(\text{theor})$ for the ith station and the jth event. The relative travel time residual is $r_{ij} = t_{ij} - \bar{t}_j$ for a given event, where the mean residual $\bar{t}_j$ is the average of observed arrivals for event j (Evans and Achauer, 1994). The mean relative teleseismic travel time residual r_i is the average of all relative travel time residuals (i.e. Ellsworth and Koyanagi, 1977; Reasenberg et al., 1980). Each of the analyzed event was recorded by at least 10 stations, and most of them included over 20 stations, implying a small scatter of errors due to varying number of observations for a given event, and ruling

Fig. 2. Contours (in seconds) of the average travel time residuals, relative to the network average, for all the events regardless of the azimuth. Positive (solid line) and negative (dashed line) relative travel time anomalies represent delayed and early arrivals, respectively. The cross-section A–A1 of Ten Brink et al. (1990) is reinterpreted here. Cross-section B–B1 is that of Hofstetter et al. (1991). Solid triangles represent seismic stations that were used in this study (Table 1). Thick dashed rectangle (centered at 35°E,

Table 1
Seismic stations that are used in this study; Jordanian stations are italicized

STA	LAT N	LON E	ELEV KM	STA	LAT N	LON E	ELEV KM
ADI	33.08	35.24	0.470	MBH	29.79	34.91	0.840
ARGM	32.18	35.53	0.220	MGI	32.46	35.43	0.300
ARVI	30.64	35.19	0.000	MKT	30.95	35.15	0.520
ASI	31.33	35.10	0.905	MML	32.44	35.42	0.510
ATAR	31.03	34.45	0.140	MMR	32.99	35.42	1.108
ATR	30.97	34.64	0.350	MNIT	32.46	35.04	0.118
ATZ	32.82	35.28	0.510	MOI	31.74	35.35	0.450
BGI	31.72	35.09	0.760	MSDA	31.32	35.29	0.400
BLVR	32.59	35.53	0.140	MZDA	31.31	35.36	−0.300
BRNI	32.74	35.00	0.400	NITZ	29.68	34.96	0.100
BSO	31.27	34.48	0.140	NOH	30.69	34.96	0.680
CRI	32.68	35.04	0.430	PRNI	30.35	35.00	0.410
DAYA	31.14	35.11	0.100	RAMI	32.79	35.13	0.037
DLIA	32.58	35.07	0.210	RMN	30.51	34.63	1.000
DOR	31.51	34.69	0.180	RTMM	31.05	34.68	0.259
DS10	31.60	35.40	−0.390	RVVM	31.04	34.72	0.200
DS11	31.80	35.51	−0.390	SDOM	31.08	35.39	−0.150
DS12	31.72	35.45	−0.390	SGI	30.22	34.66	0.560
DS13	31.67	35.43	−0.390	SHRT	29.59	34.94	0.380
DSD2	31.18	35.44	−0.390	SHVT	30.92	34.61	0.370
DSI	31.57	35.39	0.200	SVTA	30.93	34.62	0.370
DSI1	31.59	35.39	0.377	SZAF	30.90	34.55	0.290
GLH	32.71	35.66	0.340	TZDK	32.08	34.97	0.100
GVI	31.63	34.91	0.390	YTIR	31.35	35.12	0.900
GVMR	32.57	35.41	0.095	ZEFH	29.52	34.90	0.118
HLZ	31.60	34.64	0.100	ZELM	31.10	34.53	0.140
HMDT	32.26	35.52	0.125	ZNT	32.24	35.03	0.310
HRI	33.27	35.75	1.010	*BURJ*	32.24	35.80	1.045
HRSH	32.70	35.28	0.416	*DHLJ*	30.82	35.40	−0.080
JVI	31.93	35.35	0.690	*KFNJ*	31.86	35.68	−0.090
KER	30.99	34.49	0.360	*LISJ*	31.24	35.48	−0.320
KRPI	32.45	35.57	0.000	*MASJ*	31.73	35.72	0.822
KSHT	32.99	35.83	0.700	*MKRJ*	31.55	35.64	0.815
KZIT	30.91	34.39	0.200	*SALJ*	32.09	35.68	0.780
MAMI	32.50	35.15	0.461				

out the dependence of the average residual on any subset of stations.

2.2. Inversion methodology

In order to take account of the more subtle changes in the teleseismic residuals, we applied an inversion procedure based on the method proposed by Aki et al. (1977). Ellsworth (1977) and Evans and Achauer (1994) give a detailed description of the method and applications. The method utilizes a three-dimensional (3D) earth model that contains several horizontal layers, each is divided into many rectangular blocks.

The procedure seeks the velocity variations between the blocks so to achieve the minimization of the variance of the resulting residuals with respect to a given initial uniform velocity assigned to each layer. Outside the studied region the earth is assumed to be horizontally uniform. The method has been applied successfully in various regions, and we list several examples out of many, i.e. geothermal and volcanic areas (Ellsworth and Koyanagi, 1977; Reasenberg et al., 1980), subduction zone (Michaelson and Weaver, 1986; Engdahl et al., 1995), and in the vicinity of active faults (Achauer, 1992; Dorbath et al., 1996).

We adopted an eight-layer model (Table 2) all with

Table 2
Initial velocity model that is used in this study; thickness, length and width of each block are identical for a given layer, except the first layer

Layer	Thickness (km)	Length (km)	Velocity (km/s)
1	10	Cone	5.0
2	20	20	6.7
3	30	30	8.0
4	30	30	8.1
5	30	30	8.2
6	30	30	8.3
7	30	30	8.4
8	30	30	8.5

block thickness of 30 km except the first and the second layers with thickness of 10 and 20 km, respectively. Since the aperture of the total network is roughly a rectangle of 420×130 km^2, we limited the total depth of the model to half of the characteristic length, which is 210 km. The block configuration was chosen in order to optimize a grid in which almost each block will contain at least one seismic station. The choice of block dimensions of the first two layers (Table 2), having a thickness of 10 and 20 km representing the upper and lower crust, respectively, was constrained by the need to fit to the known crustal structure of the region. We note that the Moho boundary is clearly seen even at large horizontal distances (Ginzburg et al., 1979a,b; Shapira, 1990). Here we also based our model on the modified crustal structure following Ben-Avraham and Ginzburg (1990) and Hofstetter et al. (1991), where a substantial thickening of the sedimentary sequence was proposed. Therefore the first and second-layer with thickness of 10 and 20 km represent the average upper and lower crust, respectively. Following the procedure of Evans and Achauer (1994), we allocate a separate block to each station in the upper layer, which is actually a cone-shape block (Table 2). The upcoming rays, observed at two neighboring stations, rarely share a common cone, because they propagate in a nearly vertical direction and the station spacing is almost always larger than the thickness of the first layer. Due to limitations of computational facilities and station distribution, we could not decrease the block dimension much below the physical length of the typical spacing inside the seismic networks. Layers in the uppermost mantle or deeper are divided into $30 \times$

30×30 km^3 cubes, and in general, provide satisfactory resolution of the velocity anomaly. Below we describe a synthetic structure test that was conducted in order to demonstrate the actual resolvability.

Since each ray samples only a small number of blocks the resolution matrix is singular, a fact which may lead to unstable solution. To overcome this difficulty, we solve using the damped least squares inversion method (Aki et al., 1977; Ellsworth, 1977), in which stability is balanced at the expense of the resolution. The damping factor, θ^2, is approximately equal to the ratio between the estimated data variance and the variance of the model (Aki et al., 1977). One has to choose carefully the damping factor in order to optimize the inversion procedure. The stability of the solution and the dependence of the results were examined in a series of tests (Evans and Achauer, 1994) that included varying parameters like damping factor, layer thickness, initial velocities, block dimensions, and block configuration and location. The block configuration was displaced half block width to the sides and diagonally as well, yielding only minor changes. Damping factor value of $\theta = 0.0075$ (s/%)^2 provided a good balance between the resolution and standard errors, while large standard errors were introduced for $\theta > 0.0030$ (s/%)^2. We conducted several tests of minimizing the block size to reach the optimal configuration, without severely hampering the resolution and the stability of the solution. Most of the blocks, in this optimal configuration, had at least 30 rays crisscrossing through them, except at the outskirts of the model. Data uncertainty is estimated by the data variance remaining after the inversion. Variance improvement due to the assigned model is 51%.

Any inverse solution has an inherent non-uniqueness that is indicated by the resolution matrix (Aki et al., 1977; Ellsworth, 1977; Evans and Achauer, 1994). The inversion of the combined data of DSRN provides a high-resolution image of lateral variations in the velocity structure of the Dead Sea region. Resolution values ≥ 0.7 are considered good, values between 0.5 and 0.7 are considered poor, and we ignore blocks with resolution values of less than 0.5. For providing a more complete picture, only in the first layer we present the peripheral blocks with resolution values of 0.4 –0.5, though their weight in the interpretation is small.
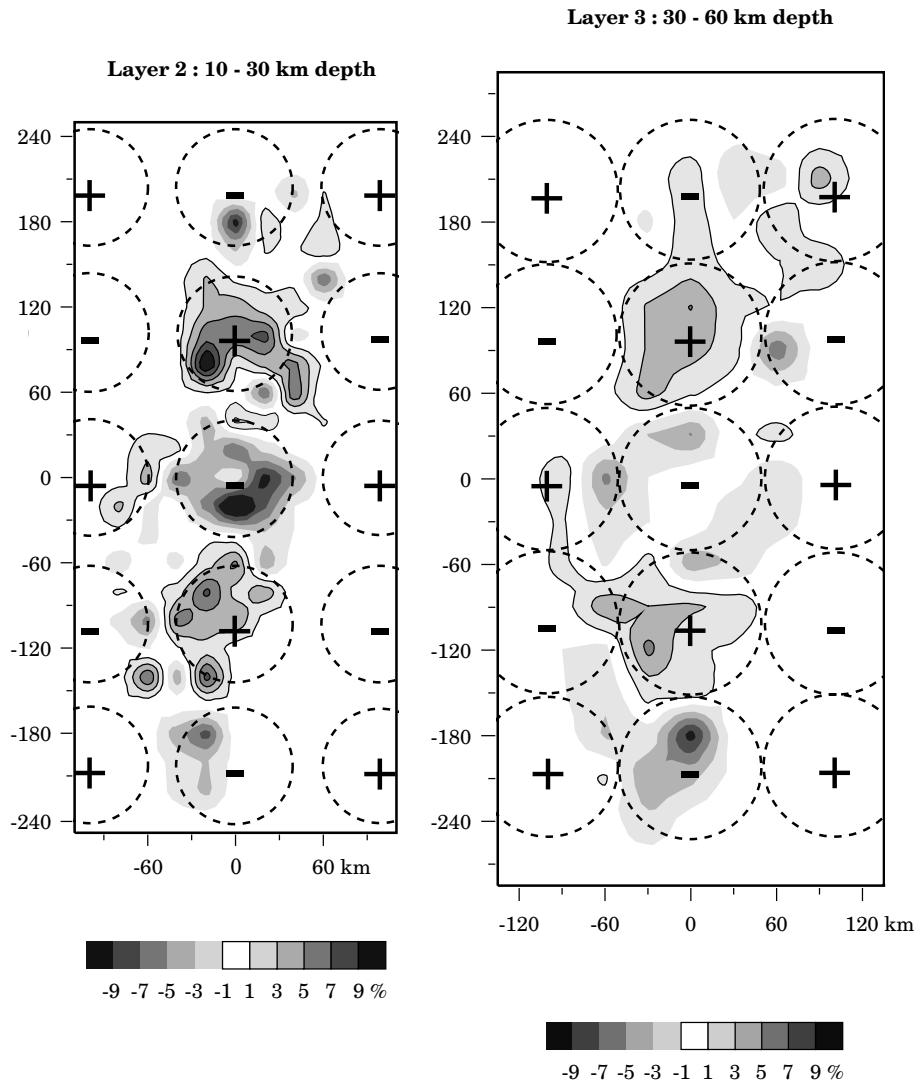
Fig. 3. Velocity changes (in percent) obtained from the application of the synthetic structure test at various depths: layer 2 at 10–30 km and layer 3 at 30–60 km.

2.3. Synthetic structure test

We have constructed a checkerboard resolution test case, similar to the procedure proposed by Humphreys and Clayton (1988) and Wittlinger et al. (1998). In this test, we assign alternating positive and negative velocity perturbations to a 3D grid, having roughly the typical size of some of the anomalies under study. Using 3D ray tracing we estimate the test residual data that correspond to the ray paths. The solution of the inversion of the residual data is then compared with the original checkerboard velocity model, which provides an estimate of the resolving power of the dataset. In this case the crust and the upper mantle are composed of spheres, each has a 50 km radius and a velocity contrast of 8% in the center, gradually decreasing towards the border (Fig. 3a). The first layer of spheres has its center at a depth of 50 km. A sphere

with an −8% velocity perturbation is situated at the center of the inversion model, being surrounded with alternating +8% and −8% spheres. A second layer of spheres, with the same radius but opposite velocity perturbation, is located immediately below the first layer. We used the same teleseismic ray dataset as we used in the tomographic study and we calculated the synthetic travel time residuals at each station. These synthetic residuals were inverted using the same initial model (Table 2). We largely recover the initial model that we used for these synthetics, i.e. layer 2 at 10–30 km depth and layer 2 at 30–60 km depth (Fig. 3). The maximal amplitude of perturbations is not recovered, but the position of the anomalies has not changed and the vertical alternate of the positive and negative perturbations is clear.

3. Results

3.1. Relative teleseismic travel time residuals

The average relative travel time residuals obtained by the DSRN using all the events are shown in Fig. 2. Because of the wide range of azimuths and incidence angles, the travel time residuals reflect an over whole characterization of the relative velocity variations under the DSRN. The general pattern is similar to that presented by Hofstetter et al. (1991). However, in this study, there is a larger number of events and recording stations for each event, and a better station distribution. Consequently, we describe here briefly only the average of all the relative travel time residuals, and we avoid further detailed discussion.

The travel time residuals are actually a summation of all the anomalies seen by the upgoing ray from the bottom of the model to the top. However, based on the inversion results presented below, one can largely interpret the residuals as a result of the changes in the upper crust. Two main points are worth mentioning here. The first relates to the DST that is of particular interest. Stations situated inside the transform observe positive anomalies, with the largest in the Southern Dead Sea basin (SDSB; dashed-line rectangle in Fig. 2). Similarly, east of the DST, although limited to a small number of stations that are located off the transform, the anomaly is positive almost

everywhere with maximum values of 0.3–0.5 s values.

The second point relates to variation of the travel time residuals west of the DST. In general, it is possible to define two main provinces in the teleseismic residual maps (Fig. 2). The first province occupies the northern part of Israel, north of about 32.2°N, and is characterized by mainly local positive residuals, generally having an east–west trend. A second province occupies most of the southern part of Israel, south of 32.0°N, and has a relatively flat residual signature with low positive or negative values, except the SDSB. The boundary between the northern and the southern provinces is a rather elongated low extending from the Mediterranean Sea to the DST. The variation of the travel time residuals, especially in the northern province, probably indicates the changes in the sedimentary sequence. Approximately the same NNW–SSE trend and northward thickening of the sedimentary sequence was indicated by several other studies based on gravity and magnetic data (Folkman and Bein, 1978; Folkman, 1980), reflection data (Frieslander et al., 1990), and geological data (Hirsch and Picard, 1988; Lewy, 1991). East of the DST the teleseismic travel time residuals are rather scarce and reveal no clear view.

3.2. Inversion results

The new contribution of this study is the application of inverse theory, using the teleseismic travel time residuals, to obtain the velocity perturbation beneath the DSRN. The results of the inversion are given in terms of velocity change from the initial velocity model (Table 2), in percent, where positive and negative values indicate higher and lower velocity, respectively (Fig. 4). Below we examine several prominent velocity perturbations that are of tectonic significance. We pay a special attention to anomalies that are located in the upper three layers (Table 2), representing the averaged upper crust, 0–10 km, lower crust, 10–30 km, and upper part of upper mantle, 30–60 km (Fig. 4A–C).

All the seismic stations, except those at the SDSB (dashed-line rectangle, Fig. 4A), are located at the outskirts of the DST. Moreover, several stations, i.e. those that located close to the Gulf of Aqaba/Eilat or the northern part of the Dead Sea basin, are situated on
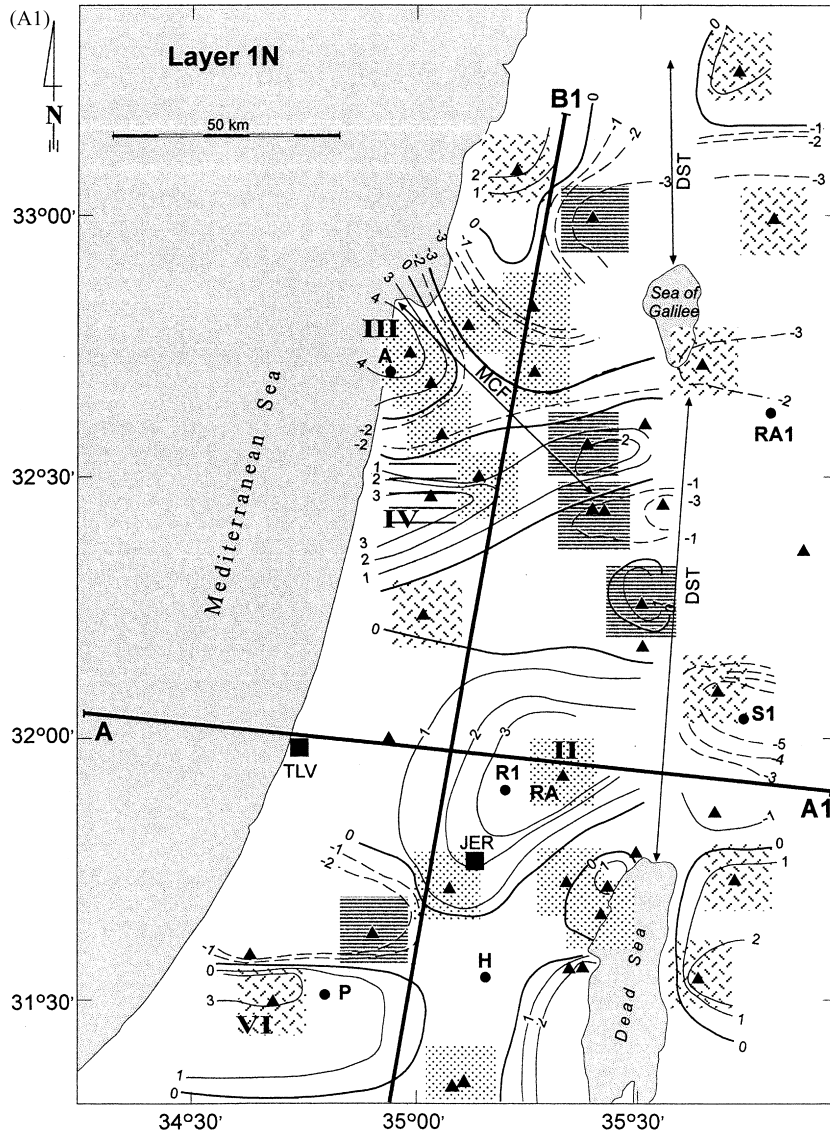
Fig. 4. Contours of smoothed velocity changes (in percent) from inversion of teleseismic residuals (map view). Fast and slow velocities are presented by solid line and dashed line, respectively. Resolution is presented in the hatched background by lines for values of 0.5–0.7 and dots for values 0.7 and up. In the first layer the short lines present additional resolution values of 0.4–0.5. Major tectonic structures, presented only in the first layer and referred to in the text, are (from north to south): DST — DST, MCF — Mt. Carmel Fault, RA — anticline of Ramallah, RC — Mahmal Ridge and Ramon Crater, KA — Karkom Graben, and PF — Paran Fault. Boreholes locations are (solid circle; from north to south): A — Atlit, RA1 — Ramtha, S1 — Suwellah, R1 — Ramallah, H — Halhul, P — Pleshet, L — Lisan, AG — Agur, S — Sodom, and RN — Ramon. Cross-sections A–A1 and B–B1 are as in Fig. 2. Solid triangles represent seismic stations that were used in this study (Table 1; only in the first layer). Thick dashed rectangle (centered at 35.5°E,31.1° N) delineates the SDSB. Solid squares represent main cities: AQ — Aqaba, EIL — Eilat, JER — Jerusalem, TLV — Tel Aviv. Depths of layers are: (A) Layer 1 (N — North, S — South), 0–10 km; (B) Layer 2, 10–30 km; (C) Layer 3, 30–60 km; (D) Layer 4, 60–90 km; (E) Layer 5, 90–120 km; (F) Layer 6, 120–150 km.
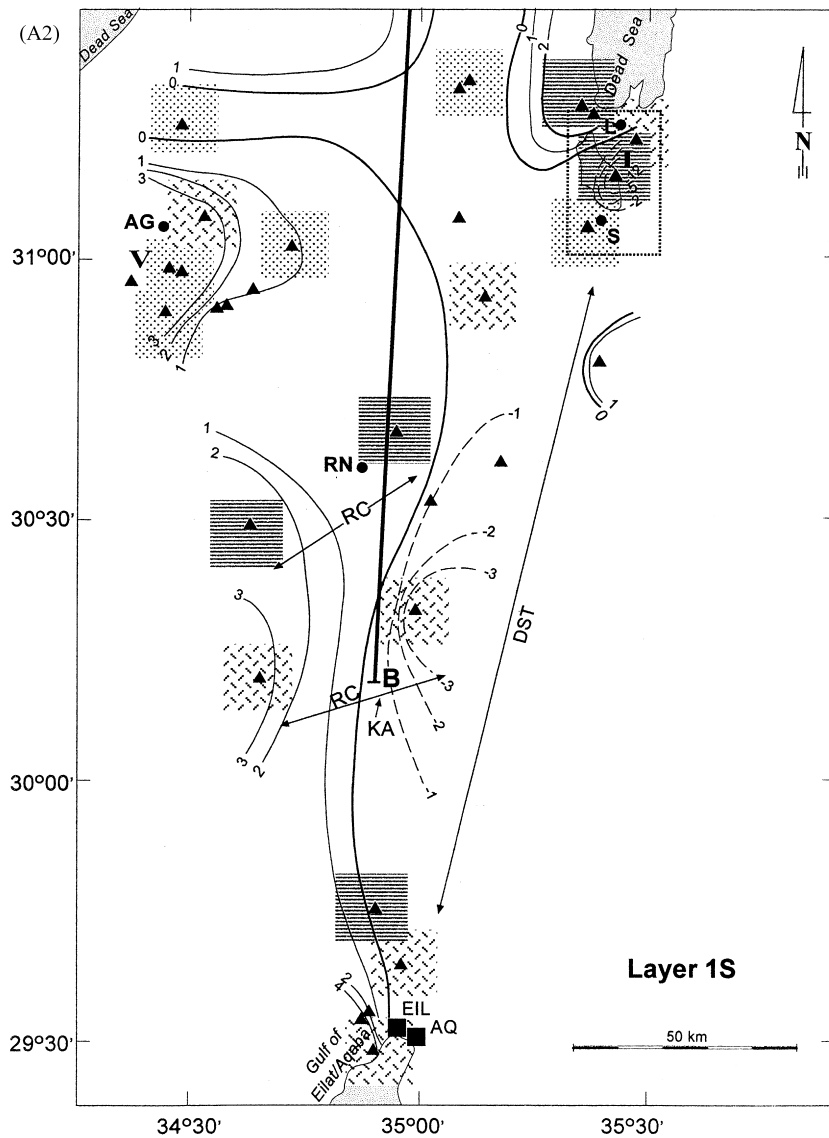
Fig. 4. (*continued*)

the bordering rocky cliffs of the transform. The obvious density difference between those sites and the sediments inside the DST causes somewhat sharp gradients of the velocity anomalies. Thus we avoid in the first layer crossing of the DST with the contours of velocity changes, except at the SDSB basin.

Referring to the first layer, the DST is mainly characterized by negative velocity anomalies to various degrees, depending on the locality (Fig. 4A). Special attention should be given to the SDSB, bounded between longitudes 35.4°E and 35.6°E and latitudes 31.0°N and 31.2°N (Fig. 4A). Borehole L, which roughly marks the northern border of the SDSB, is located in the Lisan peninsula that was a peninsula until recently and now a land strip bisecting the Dead Sea basin into the northern and southern basins (Fig. 4A). Borehole S is located in Mt.
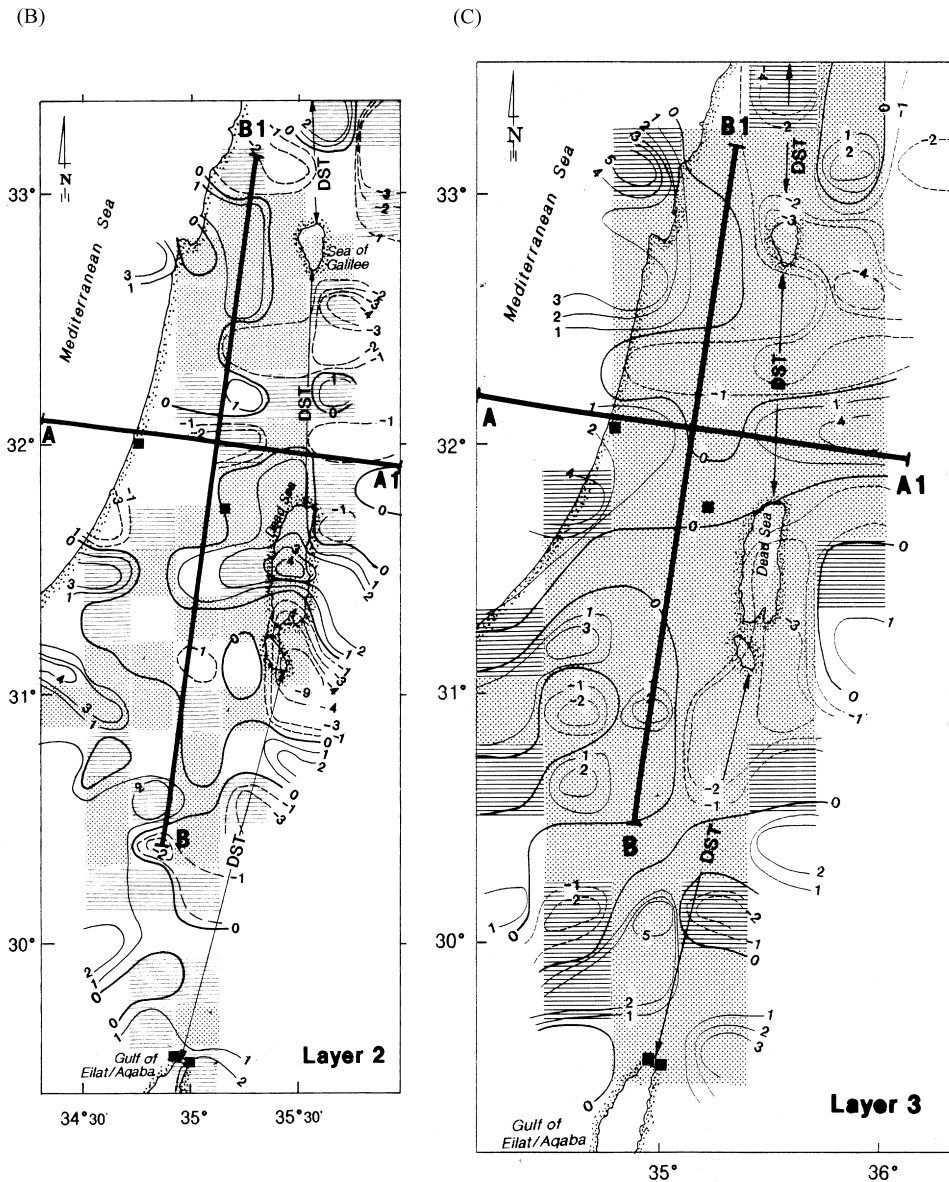
(B)

(C)

Fig. 4. (*continued*)

Sodom, a prominent salt dome, which marks the southwestern border. The SDSB is characterized by the largest negative anomaly of over −12% (anomaly I in Fig. 4A). The location of this anomaly is in excellent agreement with the location of the travel time residual anomaly (Fig. 2). Indeed, the extension of this negative velocity anomaly into greater depths, in the SDSB, is clearly visible in the second layer

(Fig. 4B), where its magnitude reaches a value of over −9%.

Besides the large velocity anomaly of SDSB there are several other prominent velocity anomalies with smaller magnitude (Fig. 4). Worth mentioning are several apparent anomlaies in Fig. 4A, i.e. the anomaly over the Ramallah anticline (anomaly II), anomalies III and IV over the Mt. Carmel, with an
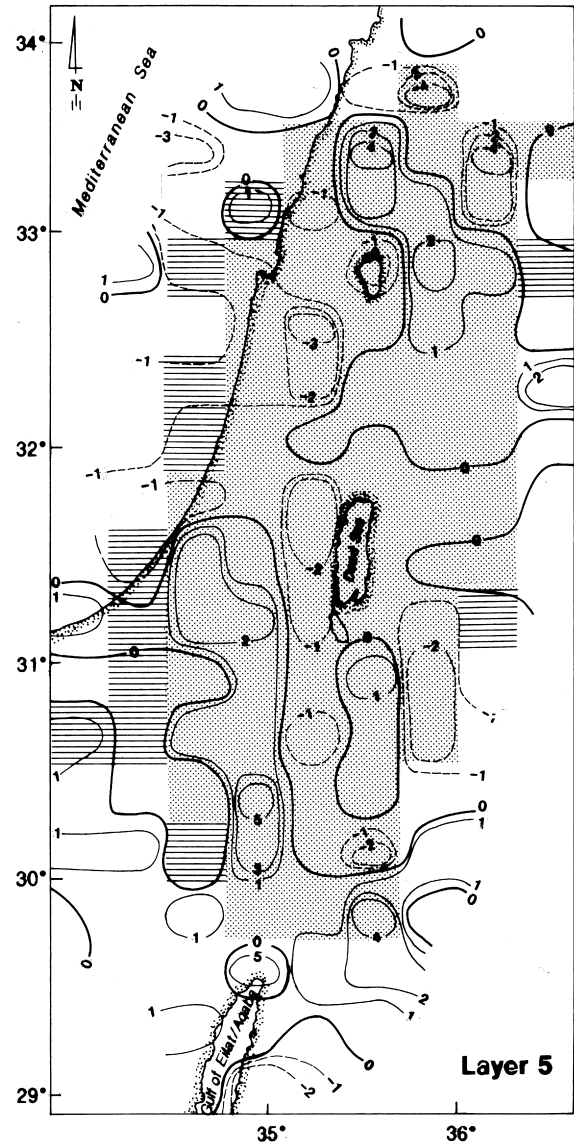
(D)
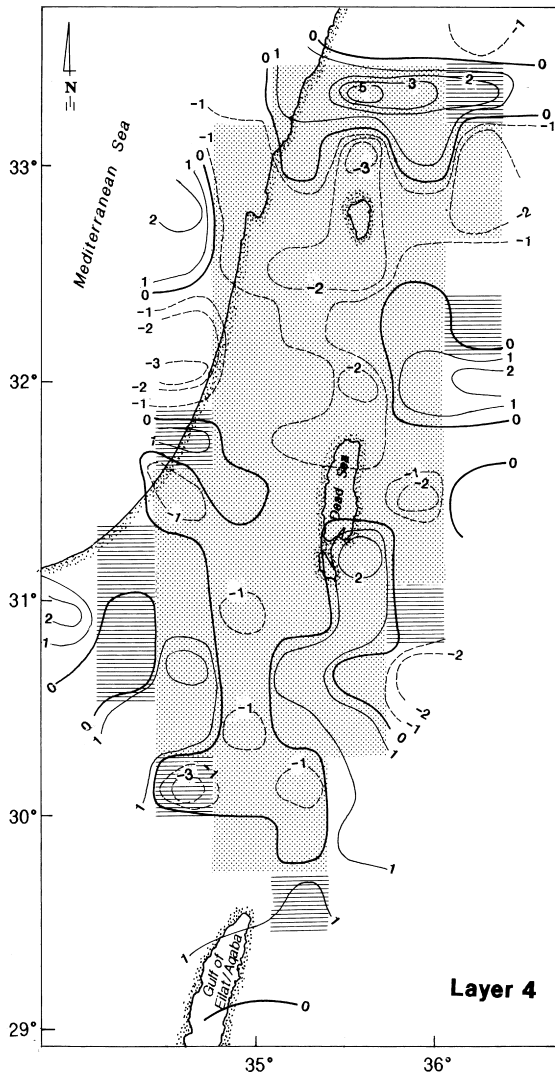
(E)

Fig. 4. (*continued*)

absolute magnitude of 3–4%. North and south of the Dead Sea basin almost all stations are located off the main transform (Fig. 4A), having small anomalies that probably reflect the local structure underneath the station. Several of these anomalies have deeper roots that extend into the second layer or the lower crust, with varying small magnitudes (Fig. 4B). In the third layer, immediately below the Moho discontinuity (Fig. 4C), we find that along the Dead Sea rift there are mostly negative velocity anomalies, i.e. the Dead Sea basin, the Sea of Galilee basin, while parts of the sides of the rift are characterized by rather small positive anomalies.

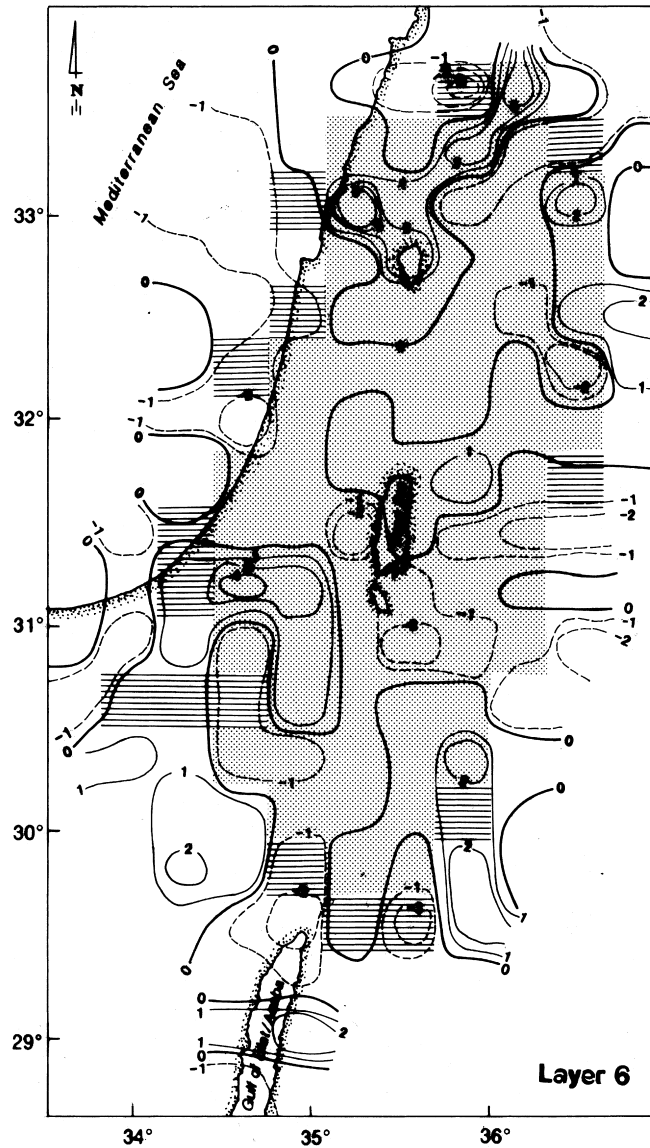In layers 4 and 5 (Fig. 4D and E) we can find

(F)

Fig. 4. (*continued*)

anomalies that may indicate a connection to the rifting of the Dead Sea. The anomalies are mainly negative, with some positive "hills" in parts. We can speculate that these anomalies are connected to some heavy material, however, neither heat flow (Feinstein, 1987) nor gravity (Rybakov et al., 1997) can support any substantial magma ascending on a regional scale.

Layers 6–8 (Fig. 4F–H) present anomalies below the continental lithosphere, assuming the latter has a thickness of 100 km. The anomalies are mainly positive under the region of the Dead Sea rift, especially in layers 7 and 8. The anomalies cannot be correlated with either the obvious gravity or magnetic anomalies or the surface topography. Most of the rugged hilly

picture in each layer is probably a function of the density or velocity changes in the upper mantle.

4. Discussion and conclusions

For a better understanding of the source of the velocity perturbations we utilize in addition relative travel time residuals (Fig. 2), Bouguer gravity data (Fig. 5), and deep borehole sections wherever available (Figs. 4A and 5). First we present an overall view of the results, and then, in the following sections, we discuss in detail several major velocity anomalies and their tectonic significance.

The first and second layers appear to be sub-divided into several structures, i.e. the Dead Sea basin or Mt. Carmel fault (Fig. 4A), with no obvious major trend that overlays the whole region. We show that the main velocity anomalies are well bounded within the changes of subsurface geology as revealed in the borehole observations (Figs. 4A and 5). The Bouguer gravity anomaly is actually the summation of all the mass density changes from the bottom of the model to the top. The Bouguer gravity anomaly is considerably influenced by the existence of thick young sediments (Rybakov et al., 1997), to be discussed below. It is worth mentioning that roughly south of about 31.7°N there is a general correlation between the trend of the major structural features as revealed in the velocity anomalies (Fig. 4A) and features of Bouguer gravity anomalies (Fig. 5). North of 31.7°N the similarity is hampered due to several reasons. Perhaps the most important influence is due to the thick sediments in the northern part of Israel mainly along the Mediterranean shore (Rybakov et al., 1997). In this case, the summation character of many mass density changes is reflected in the Bouguer gravity anomaly (Fig. 5), while velocity anomalies in Fig. 4A describe only changes in the first layer. We stress that rays travelling through the first layer are actually sampling the local changes underneath the seismic stations, and are not influenced by off-station sedimentary sequence. This in turn supports the view that the main velocity anomalies correlate with changes of subsurface geology.

A good general correlation exists between the velocity perturbations especially in the first layer (Fig. 4A) and the features observed in the teleseismic travel time residuals (Fig. 2). It means that although the travel time residuals are the summation of all the travel time changes starting from the bottom of the model to the top, the main contributions to these variations are in the crust and especially in the upper crust.

On both the northern and southern sides of the SDSB, the absolute values of the velocity anomalies are significantly low, contrary to the velocity anomaly in the center, and even slightly positive in some parts of the Lisan. The Sodom and Lisan deep boreholes (S and L in Fig. 4A) show thick layers of salt of at least 1 km and well over 4 km, respectively (Garfunkel and Ben-Avraham, 1996). Salt, despite its relatively low mass density, usually has an usually high-seismic velocity comparable to dolomite (Dobrin, 1952), and, thus, one would expect small or no anomaly in the case of a station situated above the salt dome (Fig. 4A; stations LISJ and SDOM in Table 2). Due to compaction, density log in the Sodom deep borehole shows a gradual increase of the mass density from a value of $2100 \, kg/m^3$ close to the surface to about $2400–2500 \, kg/m^3$ at depths of 4–5 km, and then it almost levels to depth of 6.5 km (bottom of borehole). Throughout the entire borehole the mass density is definitely lower than a comparable dolomite and limestone column. We assume that this column represents the cross-section within the SDSB, except for the excess of salt at the upper part that is typical in the Lisan and Mt. Sodom.

The location of the large negative velocity anomaly in the SDSB Sea basin is in excellent agreement with the center location of the Bouguer gravity anomaly change of about 75–80 mgal (Ten Brink et al., 1993; Rybakov et al., 1996,1997; Fig. 5). In addition, geological data (Kashai and Crocker, 1987), and reflection studies (Ten Brink and Ben-Avraham, 1989) indicate the existence of a very thick layer of low-density material. Ten Brink et al. (1993) interpreted the gravity anomalies as a result of low-density fill made mostly of evaporites (i.e. salt), and not specifically of clastic material. On the other hand, Rybakov et al. (1996, 1997) suggested mostly clastic material with a thickness of at least 10 km. Based on refraction data Ginzburg and Ben-Avraham (1997) observed a sedimentary sequence with a total thickness of up to 14 km, where the light material constitutes almost half of the column. The fact that both travel time residuals
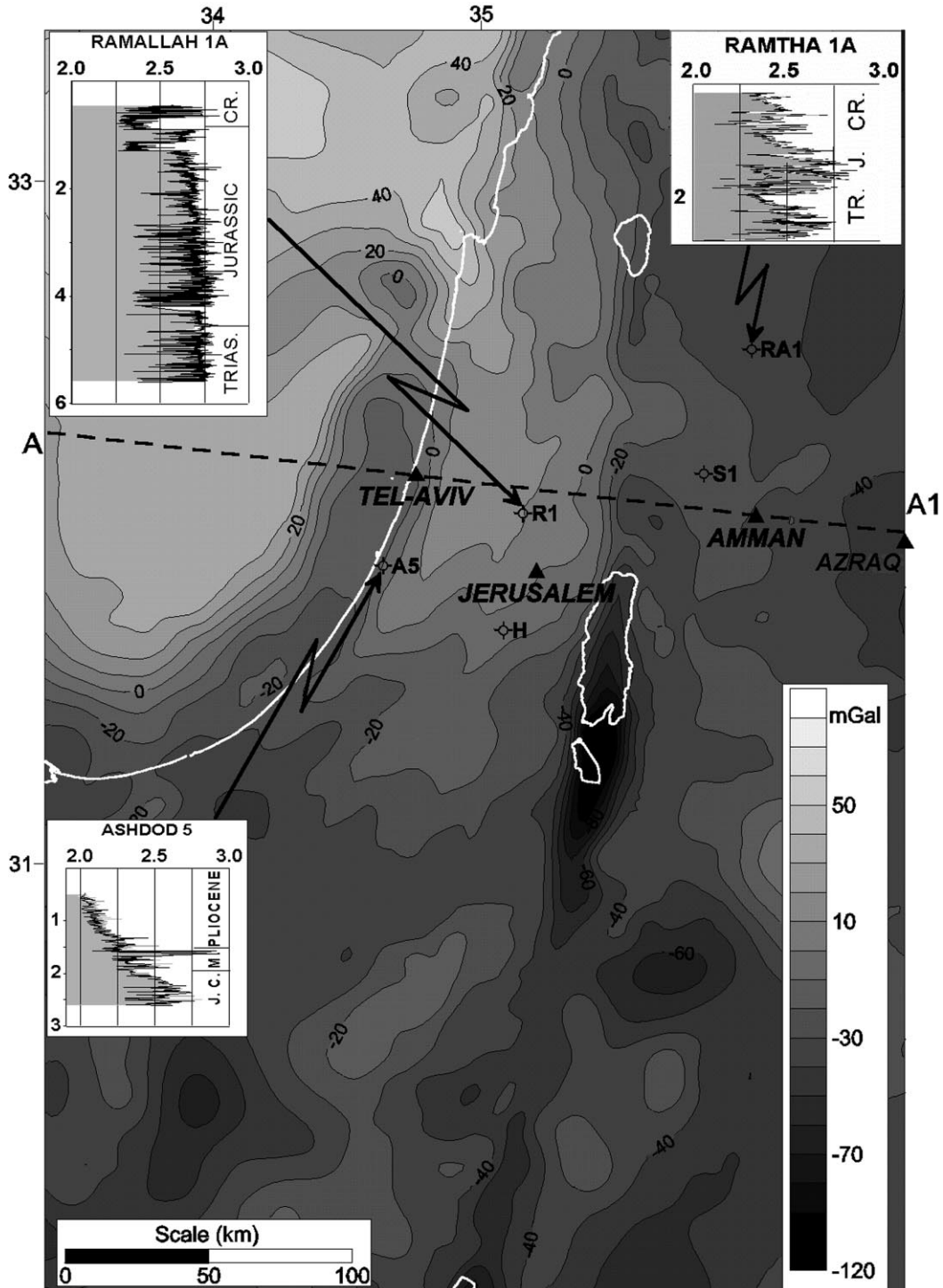
Fig. 5. Map of Bouguer gravity anomalies of Israel and its vicinity (after Rybakov et al., 1997). Contour interval is 10 mgal. Superimposed with a few typical density logs explaining some of the gravity features corresponding to shallow geological structures. The cross-section A–A1 is the location of a profile interpreted by Ten Brink et al. (1990) and reinterpreted here. The boreholes are designated by: A5 — Ashdod5; R1 — Ramallah; RA — Ramtha; S1 — Suwellah. The density log of Halhul borehole (H; Fig. 4; not shown) is similar to that of Ramallah borehole.

and velocity anomalies within the basin are suggesting slow material, relative to the ambient material, excludes the salt as a main component of the basin fill. It is possible that the large velocity anomaly, in the second layer, just below anomaly I in the first layer, is caused by the presence of lighter material, relative to the ambient material.

The positive anomaly in the Northern Dead Sea basin can be attributed to small changes of the depth of the Moho discontinuity. Based on gravity data, Ten Brink et al. (1993) suggested that no or negligible elevation of the Moho discontinuity. In accordance with the gravity data, qualitative estimation of the Moho uplift, based on the inversion of teleseismic and relative travel time anomalies, suggests that a relatively small elevation of less than 3 km can explain the positive anomaly.

Although poorly resolved, the negative velocity anomaly at 35.6°E, 32.1°N east of the DST (Figs. 2 and 4A) is in good agreement with the regional stratigraphy of the relatively low-density sandstone sequence found in Suwellah borehole S1 and in Ramtha borehole RA1 (Fig. 5; Bender, 1974; Abu Saad and Andrews, 1993). Due to the small number of stations we cannot define the regional extent of the sandstone sequence. The poorly resolved positive anomalies east of the northern Dead Sea basin (35.6°E, 31.6°N, Figs. 2 and 4A) are probably correlated with magmatic activity and perhaps some deep voluminous intrusions, based on Miocene to recent magmatic outcrop (Bender, 1974) and aeromagnetic observations (Hatcher et al., 1981).

The positive velocity anomaly II (Fig. 4A) covers the Ramallah anticline, and can be seen in the teleseismic residual map (east of AA1 and BB1 crossing point; Fig. 2) and the Bouguer gravity map (Fig. 5) as well. Deep borehole measurements there (Ramallah borehole, Figs. 4 and 5) indicate the existence of a thick layer of dolomite and carbonate sequence (>1 km), that is a characteristic late Triassic and early Jurassic great lateral extent, following a NNE–SSW trend (Cohen, 1988; Hirsch and Picard, 1988). Although this sedimentary sequence has a wide regional extent, and can be essentially viewed as the baseline, only several anomalies appear to stand out clearly, i.e. anomalies II, and III and IV to be discussed below. In other parts it is partially masked or blurred probably due to local changes, i.e. south-

west of the Sea of Galilee. The mass density increase of about 100 kg/m^3 (Ramallah borehole in Fig. 5) yields a Bouguer gravity anomaly change of about 10 mgal, in good correlation with the Bouguer gravity map (Fig. 5; Rybakov et al., 1997).

Anomalies III and IV are correlated with the thick Mesozoic carbonate sequence of Mt. Carmel that is apparent in Atlit borehole (Borehole A in Fig. 4A). There are several velocity anomalies located in the lower crust, and in the upper mantle, that are shifted north or west relative to anomaly III (Fig. 4B–D). All anomalies, except the one below anomaly III in the upper mantle (Fig. 4A and C), are poorly resolved, and thus their weight in the interpretation is minimal. The anomalies possibly reflect some magmatic bodies or the ascending of heavier material, whose origin is unclear. Recently Rybakov et al. (1995a, 1996) studied the effect of the near shore young sediments and the Asher volcanic sequence (Atlit borehole A, Fig. 4; Klang, 1983a,b; Gvirtzman et al., 1990) on the Bouguer gravity anomaly. They found that if one replaces the Asher sequence and the light sediments near the shore, with the carbonate mass density typical to the Mt. Carmel sequence, the Bouguer anomaly is essentially canceled out.

The velocity anomalies in the upper crust in the vicinity of the Halhul borehole (borehole H in Fig. 4A; located at 35.2°E and 31.5°N) west of the Dead Sea basin, are slightly negative with rather complex overall shape. In this borehole section no special mass density changes are observed. The average travel time residuals are somewhat positive pointing to slightly slow material in depth., and no apparent Bouguer gravity anomaly (Fig. 5) can be seen in its vicinity. In contrary, this region is characterized with a large and wide magnetic anomaly, where borehole H is roughly located close to its center. Recently Rybakov et al. (1994, 1995b) examined this pronounced magnetic anomaly, and suggested a wedge-like northward thinning magnetic body, located deeper than the bottom part of borehole H, that can model the observed anomaly. Based on all the above mentioned observations, it is likely that this body is composed of volcanic material with mass density probably slightly lower than the ambient material, as suggested also by Rybakov et al. (1995b).

The positive anomalies V and VI, close to the Mediterranean Sea (Fig. 4A), that can be observed

on the magnetic map (Rybakov et al., 1994), are not apparent in the Agur and Pleshet deep boreholes (Fig. 4A). The anomalies are probably associated with some relatively fast material at depths of 5–10 km that may possibly extend into the lower crust (Fig. 4B). Further south, the location of the travel time residuals and velocity anomaly close to the Gulf of Eilat/Aqaba (Figs. 2 and 4A) are well correlated with the exposed crystalline outcrop that has higher mass density (Dobrin, 1952) than the first-layer sediments inside the gulf.

The Ramon Crater (RC, Fig. 4A), approximately 40 km long erosive valley in which Mesozoic volcanic are exposed, is situated in a SW–NE elongated asymmetric ridge known as the Mahmal, which is by itself a prominent topographic feature. The positive velocity anomalies over the ridge (centered at about 34.8°E, 30.6°N; Fig. 4A and B) in the first and second layers is relatively moderate. The increase in the Bouguer gravity anomaly of about 10 mgal is rather small (Fig. 5). In the Ramon borehole (Fig. 4A) there is a small mass density increase (density log is not shown). The magnetic anomalies over the Ramon crater and its vicinity are characterized by changes on a scale of about 10 km (Rybakov et al., 1994). Relatively shallow small size bodies, perhaps composed of crystallized magma, probably cause all these anomalies. South of the Ramon feature, the negative velocity anomaly in the second layer (Fig. 4B) is correlated well with the Karkom graben (KA, Fig. 4A) that constitutes a part of the Paran fault. Despite the poor resolution, a possible explanation of the anomaly is the subsidence of lighter material in the graben, relative to the ambient material. There is no seismic station in the graben to determine upper layer velocity, however, regional mapping indicates a few kilometers of sediments (Weissbrod and Klang, 1974) in good agreement with the second-layer anomaly.

4.1. On the depth of the Moho discontinuity

Seismic refraction studies (Ginzburg et al., 1979a,b; Ginzburg and Gvirtzman, 1979; Ginzburg and Folkman, 1980; Makris et al., 1983; El-Isa et al., 1987), and regional studies using gravity data (Folkman, 1976; Ten Brink et al., 1990; Eppelbaum and Pilchin, 1994) illustrate sedimentary and crustal

sections on opposing sides of the Dead Sea rift. Recent compilation of gravity and magnetic maps (Rybakov et al., 1997) supports the view that Israel is a transition zone between the oceanic or intermediate crust of the Eastern Mediterranean Sea (Makris et al., 1994) and a thicker crust of Jordan (El-Isa et al., 1987; El-Isa, 1990). Moreover, Rybakov et al. (1997) suggested that the DST probably marks an extinct crustal boundary. Eppelbaum and Pilchin (1994) compiled the regional Moho discontinuity map using the Bouguer gravity anomaly and deep seismic refraction data. The Bouguer gravity map (Fig. 5; Rybakov et al., 1997), however, reflects the gravity effects of not only the Moho discontinuity but also of the young (post-Turonian) sediments of the Eastern Mediterranean. The maximal thickness of these light sediments, with mass density values of 2000–2500 kg/m^3, was obtained from a borehole section of Ashdod 5 (Fig. 5) and Cohen (1988). The Bouguer gravity anomalies caused by these sediments, reach −50 mgal, and therefore the gravity signature significantly masks the gravity influence of the Moho discontinuity. In order to discern the gravity anomalies associated with the denser rocks, we calculated the effect of the overlying post-Turonian sediments and then removed it from the overall anomaly. The calculations have been carried out on a 3D model taking into account the thickness of the young sediments from the base of the Senonian. Fig. 6 presents the new regional replaced gravity map, which is considerably different from the original Bouguer map (Fig. 5). The replaced gravity displays far better the deep structures in the area, i.e. Fig. 7C illustrates the crustal model and replaced gravity along the cross-section A–A1 (Fig. 2).

We calculated the correlation between the depth of the Moho as provided by seismic data (Ginzburg et al., 1979a,b; Ginzburg and Folkman, 1980; Makris et al., 1983), teleseismic based profiles (Hofstetter et al., 1991) and gravity anomalies (Rybakov et al.,1997). The empirical distribution of the Moho depth-regional replaced gravity data (Fig. 6C) suggests a parabolic correlation such as:

$$H = -33.87 + 0.19g - 10^{-3}g^2 + 2 \times 10^{-6}g^3$$

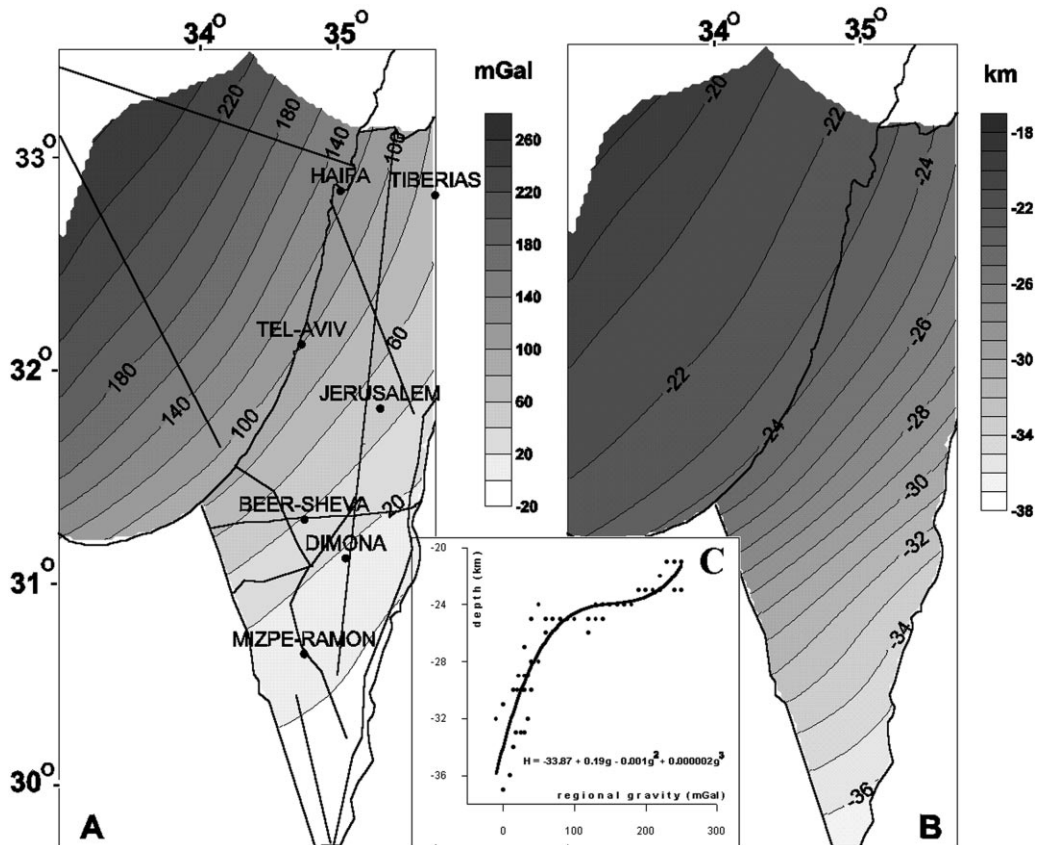where H is the depth (in km) of the Moho and g is the regional replaced gravity (in mgal). This surface can

Fig. 6. (A) Regional replaced gravity map. Contour interval is 20 mgal. Lines show seismic refraction or teleseismic profiles used in this study. (B) Depth of Moho discontinuity in kilometers. (C) Depth-gravity correlation with best fitting curve.

serve as a good approximation of the "reference Moho", had there no density anomalies or tectonic processes. Offshore Israel the pattern of the Moho discontinuity suggests a slightly deepening Moho surface, with an average southward deepening slope of about 1/40, and high replaced gravity values. The Moho deepens relatively steeply inland with an average slope of about 1/12, associated with lower replaced gravity due to the thick sedimentary sequence and large Moho depth values.

4.2. Application of teleseismic observations and Bouguer gravity anomalies to two cross-sections

The locations of the cross-sections B–B1 and A–A1 are presented in Fig. 2 and are identical to those presented by Hofstetter et al. (1991) and Ten Brink et al. (1990), respectively. First we discuss observations

along cross-section B–B1 (Fig. 7A). The procedure of the calculation of the teleseismic travel time residuals and results presented in Fig. 2 are similar to those of Hofstetter et al., 1991; Fig. 4). We assume that large undulations of the Moho discontinuity are unlikely, i.e. Ginzburg et al. (1979a,b) and Ginzburg and Folkman (1980) found along the latitude 33°N a Moho depth difference of up to 8 km between the Dead Sea rift (~30 km) and about 20 km west of the rift (~22 km). Thus we keep the Moho discontinuity between 25 and 30 km, and assume a deepening of the top crystalline basement to about 13 km. Along cross-section B–B1 we get calculated travel time residual difference of about 0.35 s, which is in excellent agreement with the observed value (Fig. 2; see also Hofstetter et al., 1991). Along large parts of the cross-section B–B1, the travel time residuals (multiplied by −10 in Fig. 7A) are correlated with
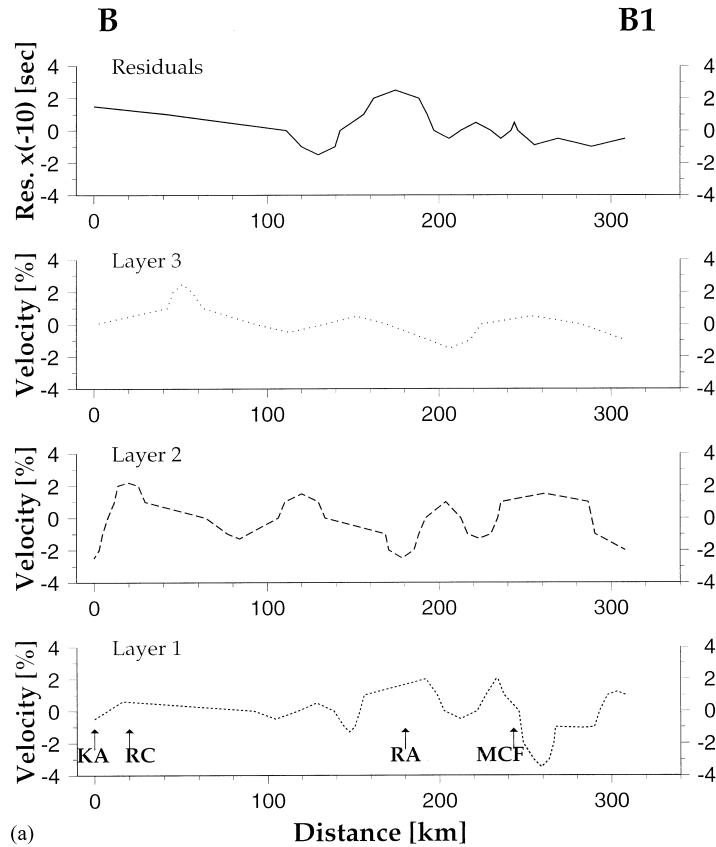
Fig. 7. Crustal model and velocity anomalies of layers 1 (short dashes), 2 (long dashes), and 3 (dots) and teleseismic travel time residuals (*r*; multiplied by −10; solid line) along the cross-sections: (A) B−B1; (B) part of the cross-section A−A1 (see also Ten Brink et al., 1990) for which teleseismic P-wave observations are; (C) best fit gravity and magnetic data for the subsurface geology along the cross-section A−A1, and the associated crustal model following Ten Brink et al. (1990) including our modifications. The locations of these cross-sections are presented in Figs. 2 and 4, along with names of major structures to facilitate the identification. In the crustal model solid lines present known boundaries, while dashed lines present assumed/calculated boundaries. Numbers in parenthesis represent mass density in kg/m^3.

the velocity anomalies, obtained from the velocity inversion of layer 1 (Fig. 7A). It implies that most of the travel time residuals can be attributed to changes in the upper crust, while probably the contribution of deep layers is small. The teleseismic data suggest that north of 32.0°N the anomalies in the northern province have a different character relative to those in the southern province. Earlier studies of Folkman and Bein (1978), Folkman (1980) and Rybakov et al. (1995a,b), using gravity and magnetic data, Hirsch and Picard (1988) and Lewy (1991) using geological data, and Frieslander et al. (1990) based on seismic reflection data, supported the idea of significant northward deepening of the top crystalline

basement, as we move from the southern to the northern province.

It is of geophysical interest to examine the differences between both sides of the DST, along cross-section A−A1 (Fig. 7B). We reinterpret the geological, gravity, seismic refraction data and teleseismic P-wave travel times along a 320-km profile running from the Mediterranean Sea, west of Tel Aviv to Azraq in Jordan, via Amman (Figs. 2, 4 and 7B), which is the same profile of Ten Brink et al. (1990). Since the eastern side of the DST has higher topographic altitude than that across the DST on the western side of more than 700 m in several places (Wdowinski and Zilberman, 1996), one would expect
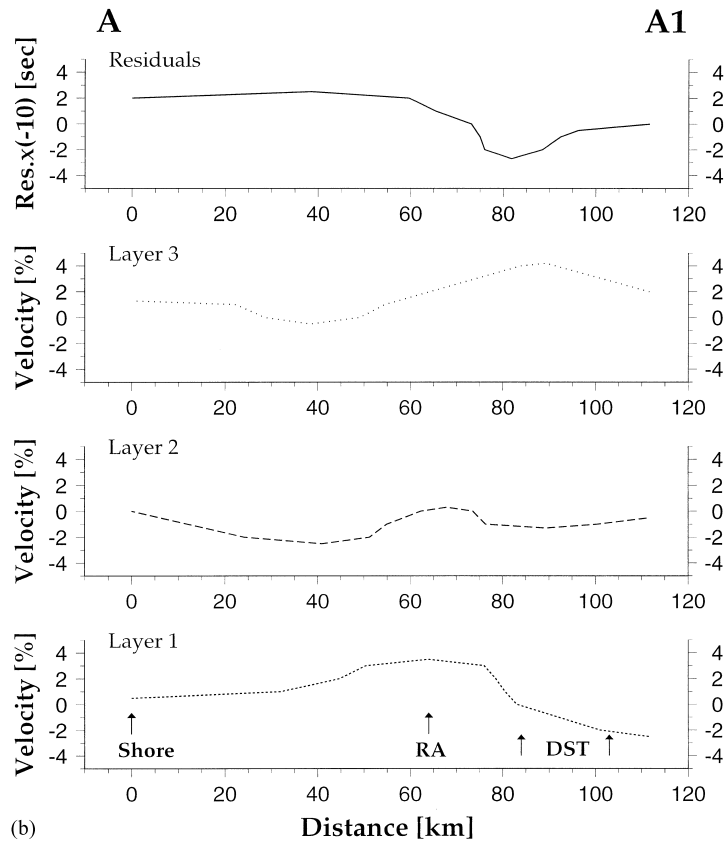
A   **A1**

(b)

Fig. 7. (*continued*)

to observe variations of geophysical parameters. Our proposed crustal model is shown in Fig. 7C, which is based in addition on borehole data and recent magnetic study (Rybakov et al., 1995a,b) as well. We show that all imply necessary modifications of the currently known crustal model (based on Ginzburg et al., 1979a,b; Folkman and Ginzburg, 1980; El-Isa et al., 1987; Ben-Avraham and Ginzburg, 1990; Ten Brink et al., 1990). First, we examine Bouguer gravity anomalies and borehole logs (Figs. 5 and 7) on both sides of the DST. The boreholes of Ramtha 1A and Suwellah S1 (Fig. 5; Bender, 1974; Abu Saad and Andrews, 1993) on the eastern DST present a sand-stone sequence above the basement with a typical mass density of 2520 kg/m^3. This is a minor replacement of the uniform 2550 kg/m^3 density used by Ten Brink et al. (1990). On the western side of the DST there is a clear appearance of a carbonate–dolomite sequence with a typical mass density of 2720 kg/m^3

(Halhul and Ramallah boreholes, Fig. 5). The heavier mass density extends northward and southward of the cross-section A–A1, and replaces the relatively lighter mass density used by Ten Brink et al. (1990). The gravity step caused by this density contrast is about 45 mgal and explains the essential part of the gravity difference across the DST. The free-air gravity anomaly in general expresses the main topographical features (Dobrin, 1952). Although the altitude of the eastern side of the DST is higher than that of the western side, still we get the opposing behavior in the free-air anomaly (Fig. 7C). This suggests a lighter mass column in the eastern side of the DST relative to that on the western side.

We assume that, in general, P-wave velocity increases proportionally with mass density and isostasy is not heavily perturbed (Fig. 7B and C). The teleseismic travel time residuals along the cross-section A–A1 (Figs. 2 and 7B), are mainly
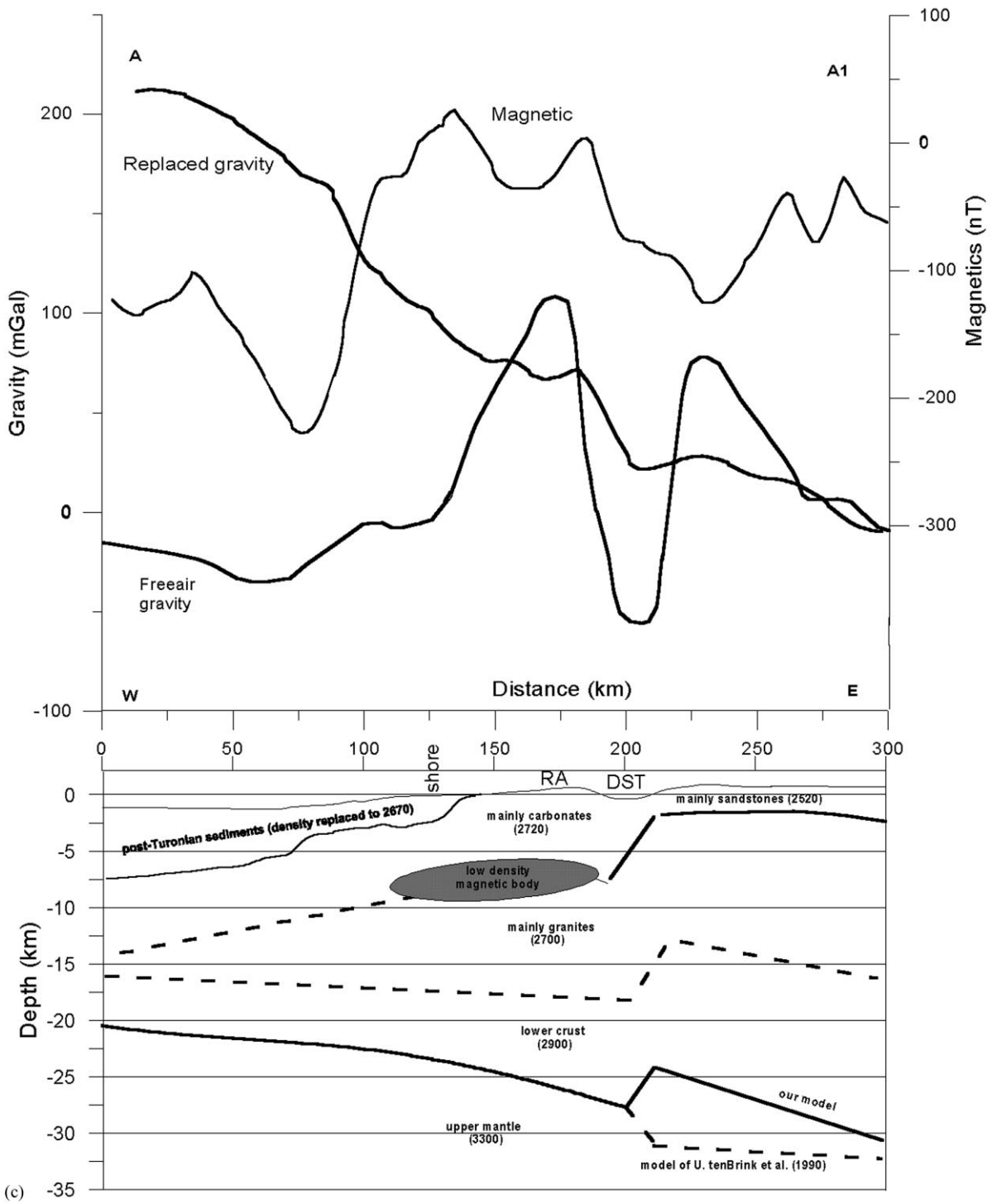
Fig. 7. (*continued*)

positive on the eastern side of the DST and negative on the western side, thus suggesting that the mass column of the eastern highlands probably contains lighter material relatively to the equivalent column across the DST on the western side. Largely, along cross-section A–A1 the teleseismic travel times residuals are negatively correlated with the velocity anomalies in the first layer (Fig. 7B). It means that large part of the travel time residuals can be related to changes in the upper crust, and the contribution of deeper layers is small. The fact that the Moho discontinuity is clearly seen over large distances in the refraction studies both in Israel (Ginzburg et al., 1979a,b) and Jordan (El-Isa et al., 1987), implies that the depth location of the Moho discontinuity in the crustal model is satisfactory. According to the model of Ten Brink et al. (1990), an uprising ray on the eastern side propagates through slower material than that on the western side at about the Moho depth while faster material at shallow depth. The net result is the partial cancellation of the travel time differences, due to the opposing effects of fast material replacing slow material and vice versa. Indeed, the total calculated travel time residuals, following the procedure presented by Hofstetter et al. (1991), due to these differences is about 0.2 s out of more than the 0.5 s of the total observed travel time difference (Fig. 7B). For a complete explanation of the 0.5 s travel time anomaly one needs to assume some eastward thickening of light material in the upper crust of Jordan.

The inversion of teleseismic P waves yields similar results. The velocity anomalies of the first layer (Fig. 4A) on the western side increase by more than 3%, while on the eastern side there is a decrease of the velocity by more than 3%. The velocity anomalies in the second layer (Fig. 4B), though they are poorly resolved on both sides, show opposing behavior to first layer. The obvious change of velocity anomalies in the first layer can be explained by a decrease of the mass density of $200 \, \text{kg/m}^3$, in the modified crustal model (Fig. 7), based on sandstone sequence in the Ramtha and Suwellah boreholes (RA1 and S1, Fig. 4A; Bender, 1974; Abu Saad and Andrews, 1993). The velocity changes in the second layer may hint to the presence of some relatively lighter material in the western mass column, probably mass density difference less than $200 \, \text{kg/m}^3$, agreeing with the

crustal model. The anomalies in the third layer, and even the fourth layer (Fig. 4C and D), suggest an increase of the seismic velocity on the eastern side, and therefore a probable increase of the mass density, though both the nature of this increase is unclear and its connection to the DST are unclear.

Our model (Fig. 7C), providing the best fit of the gravity and magnetic anomalies (Rybakov et al., 1994,1997), suggests that a change of the lower crust and mantle geometry is required in the model of Ten Brink et al. (1990). The first change is the uplift of the deep layers east of the DST, instead of the downgoing as was suggested previously. Only an uplift of about 4–5 km can produce a gravity anomaly effect which compensates for the above gravity step corresponding to the sedimentary density contrast. This uplift presents a clearer explanation of the Jordan highlands, features of the free-air gravity anomalies and the documented basement step (Fig. 7C). It is likely, though there is no clear evidence, that the total Miocene to present motion along the DST has been accompanied by an uplift of the eastern flank of the transform, pointed also by Wdowinski and Zilberman (1996).

The second change of the previous crustal model most probably corresponds to a low-density body in the central part of the profile, as appears in the replaced gravity (Fig. 7C). The magnetic anomaly located over this site is in good correlation with the regional replaced gravity. We suggest, therefore, that the object which causes both the gravity low and the magnetic high, corresponds to Mesozoic volcanism with an average mass density of about 2500–$2600 \, \text{kg/m}^3$ and high magnetization (Rybakov et al., 1995a,b).

Science Research Administration, Ministry of the National Infrastructure, Israel, the Institut de Physique du Globe, Strasbourg, URA CNRS 1358, France, and ORSTOM, France. Several of the figures were prepared using the GMT program (Wessel and Smith, 1991).

References

Abu Saad, L., Andrews, I. 1993. A database of stratigraphic information from deep boreholes in Jordan. Natural Resources Authority, Jordan, Subsurface Geology, 6.

Achauer, U., 1992. A study of the Kenya rift using delay-time tomography analysis and gravity modeling. Teconophysics 209, 197–207.

Aki, K., Christofferson, A., Husebye, E., 1977. Determination of the three-dimensional seismic structure of the lithosphere. J. Geophys. Res. 82, 277–296.

Ben-Avraham, Z., Ginzburg, A., 1990. Displaced terranes and crustal evolution of the Levant and the eastern Mediterranean. Tectonics 9, 613–622.

Bender, F., 1974. Geology of Jordan. Gebruder Borntraeger, Berlin (196pp.).

Cohen, Z., 1988. Hydrocarbon potential of Israel. Oil Exploration Investments Ltd, pp. 148.

Dobrin, M.B., 1952. Introduction to Geophysical Prospecting. McGraw-Hill, New York (435pp.).

Dorbath, C., Oppenheimer, D., Amelung, F., King, G., 1996. Seismic tomography and deformation modeling of the junction of the San Andreas and Calaveras faults. J. Geophys. Res. 101, 27 917–27 941.

El-Isa, Z., 1990. Lithospheric structure of the Jordan–Dead Sea transform from earthquake data. Tectonophysics 180, 29–36.

El-Isa, Z., Mechie, J., Prodehl, C., Makris, J., Rihm, R., 1987. A crustal structure study of Jordan derived from seismic refraction data. Tectonophysics 138, 235–253.

Ellsworth, W.L., 1977. Three-dimensional structure of the crust and mantle beneath the island of Hawaii. PhD thesis, Massachusetts Institute of Technology, Cambridge.

Ellsworth, W.L., Koyanagi, R., 1977. Three-dimensional crust and mantle structure of Kilauea Volcano, Hawaii. J. Geophys. Res. 82, 5379–5394.

Engdahl, R., Sindorf, J., Epply, R., 1977. Interpretation of relative teleseismic P wave residuals. J. Geophys. Res. 82, 5671–5682.

Engdahl, R., van der Hilst, R., Berrocal, J., 1977. Imaging of subducted lithosphere beneath South America. Geophys. Res. Lett. 22, 2317–2320.

Eppelbaum, L., Pilchin, A. (1994). New map of Moho discontinuity of Israel. Israel Geological Society Annual Meeting, Hof Ginosar, p. 23.

Evans, J., Achauer, U., 1994. Teleseismic velocity tomography using the ACH method: theory and application to continental-scale studies. In: Iyer, H., Hirahara, K. (Eds.). Seismic Tomography: Theory and Practice. Chapman and Hall, London, pp. 319–360.

Feinstein, S., 1987. Constraints on the thermal history of the Dead Sea graben as revealed by coal ranks in deep boreholes. Tectonophysics 141, 135–150.

Folkman, Y., 1976. Magnetic and gravity investigation of the crystal structure in Israel. PhD thesis, Tel Aviv University, 205pp.

Folkman, Y., 1980. Magnetic and gravity investigations of the Dead Sea rift and adjacent areas in northern Israel. J. Geophys. 48, 34–39.

Folkman, Y., Bein, A., 1978. Geophysical evidence for a pre-late Jurassic fossil continental margin oriented east–west under central Israel. Earth Planet. Sci. Lett. 39, 335–340.

Frieslander, U., Rotstein, Y., Derin, B., Trachtman, P., 1990. Paleozoic basins in central Israel. Israel Geological Society Annual Meeting, Eilat.

Garfunkel, Z., Ben-Avraham, Z., 1996. The structure of the Dead Sea basin. Tectonophysics 266, 155–176.

Ginzburg, A., Ben-Avraham, Z., 1997. A seismic refraction study of the north basin of the Dead Sea, Israel. Geophys. Res. Lett. 24, 2063–2066.

Ginzburg, A., Folkman, Y., 1980. The crustal structure between the Dead Sea rift and the Mediterranean Sea. Earth Planet. Sci. Lett. 51, 181–188.

Ginzburg, A., Gvirtzman, G., 1979. Changes in the crust and in the sedimentary cover across the transition from the Arabian Platform to the Mediterranean Basin: evidence from seismic refraction and sedimentary studies in Israel and Sinai. Sediment. Geol. 23, 19–36.

Ginzburg, A., Makris, J., Fuchs, K., Prodehl, C., Kaminski, W., Amitai, U., 1979a. A seismic study of the crust and upper mantle of the Jordan–Dead Sea rift and their transition toward the Mediterranean sea. J. Geophys. Res. 84, 1569–1582.

Ginzburg, A., Makris, J., Fuchs, K., Perathoner, B., Prodehl, C., 1979b. Detailed structure of the crust and upper mantle along the Jordan–Dead Sea rift. J. Geophys. Res. 84, 5605–5612.

Gvirtzman, G., Klang, A., Rotstein, Y., 1990. Early Jurassic shield volcano below Mount Carmel: new interpretation of the magnetic and gravity anomalies and implication for early Jurassic rifting. Isr. J. Earth Sci. 43, 21–38.

Hatcher, R., Zietz, I., Regan, R., Abu-Ajamieh, M., 1981. Sinistral strike-slip motion on the Dead Sea rift: confirmation from new magnetic data. Geology 9, 458–462.

Hirsch, F., Picard, L., 1988. The Jurassic facies in the Levant. J. Petrol. Geol. 11, 277–308.

Hofstetter, A., Feldman, L., Rotstein, Y., 1991. Crustal structure of Israel: constraints from teleseismic and gravity data. Geophys. J. Int. 104, 371–379.

Humphreys, E., Clayton, R., 1988. Adaptation of back project tomography to seismic travel time problems. J. Geophys. Res. 93, 1073–1085.

Kashai, E., Crocker, P., 1987. Structural geometry and evolution of the Dead Sea–Jordan rift system as deduced from new subsurface data. Tectonophysics 141, 33–60.

Klang, A., 1983a. Velocity survey of Atlit 1 well. Inst. Petrol. Res. Geophys. Rept. VS/841/81.

Klang, A., 1983b. Velocity survey of Atlit 1 well (phase two). Inst. Petrol. Res. Geophys. Rept. VS/842/81.

Lewy, Z., 1991. Periodicity of Cretaceous etirogenic pulses and the disappearance of the carbonate platform facies in late Cretaceous time (Israel). Isr. J. Earth Sci. 40, 51–58.

Makris, J., Ben-Avraham, Z., Behle, A., Ginzburg, A., Giese, P., Steinmetz, L., Whitmarsh, R., Eleftheriou, S., 1983. Seismic refraction profiles between Cyprus and Israel and their interpretation. Geophys. J. R. Astron. Soc. 75, 575–591.

Makris, J., Wang, S., Odintsov, S., Udintsev, G., 1994. The magnetic field of the eastern Mediterranean Sea. In: Krasheninnikov, V., Hall, J. (Eds.), Geological Structure of the Northern Mediterranean, Jerusalem, pp. 75–87.

Michaelson, C., Weaver, C., 1986. Upper mantle structure from teleseismic P wave arrivals in Washington and northern Oregon. J. Geophys. Res. 91, 2077–2094.

Reasenberg, P., Ellsworth, W., Walter, A., 1980. Teleseismic evidence for a low-velocity body under the Coso geothermal area. J. Geophys. Res. 85, 2471–2483.

Rybakov, M., Goldshmidt, V., Folkman, Y., Rotstein, Y., Ben Avraham, Z., Hall, J., 1994. Magnetic map of Israel and adjacent areas (1:500,000), Inst. Petrol. Res. Geophys.

Rybakov, M., Goldshmidt, V., Fleisher, L., 1995a. Gravity and magnetic study of the Haifa Bay area, Inst. Petrol. Res. Geophys. Rept., R12/1/95, 17pp.

Rybakov, M., Goldshmidt, V., Fleisher, L., 1995b. A new look at the Hebron magnetic anomaly. Isr. J. Earth Sci. 44, 41–49.

Rybakov, M., Goldshmidt, V., Fleisher, L., Gvirtzman, G., Goldberg, I., Sorin, V., 1996. Interpretation of gravity and magnetic data from Israel and adjacent areas: investigation results. Inst. Petrol. Res. Geophys. Rept. R04/313/95.

Rybakov, M., Goldshmidt, V., Rotstein, Y., 1997. New compilation of the gravity and magnetic maps of the Levant. Geophys. Res. Lett. 24, 33–36.

Shapira, A., 1990. A note on the apparent velocities of Pn and Sn waves across Israel. Inst. Petrol. Res. Geophys. Rept., Z1/567/79(69).

Ten Brink, U., Ben-Avraham, Z., 1989. The anatomy of a pull-apart basin: seismic reflection observations of the Dead Sea basin. Tectonics 8, 333–350.

Ten Brink, U., Schoenberg, N., Kovach, R., Ben Avraham, Z., 1990. Uplift and a possible Moho offset across the Dead Sea transform. Tectonophysics 180, 71–85.

Ten Brink, U., Ben-Avraham, Z., Bell, R., Hassouneh, M., Coleman, D., Andersean, G., Tibor, G., Coakley, B., 1993. Structure of the Dead Sea pull-apart basin from gravity analyses. J. Geophys. Res. 98, 21887–21894.

Wdowinski, S., Zilberman, E., 1996. Kinematic modelling of large-scale structural asymmetry across the Dead Sea rift. Tectonophysics 266, 187–201.

Weissbrod, T., Klang, A., 1974. Configuration of the buried surface of the Precambrian and the stratigraphy of the Paleozoic in the central Negev: indications from Magneto–Telluric measurements. Isr. Geol. Surv. Bull. 60, 14.

Wessel, P., Smith, W., 1991. Free software helps maps and display data. EOS Trans. AGU 72, 441.

Wittlinger, G., Tapponier, P., Poupinet, G., Mei, J., Danian, S., Herquel, G., Masson, F., 1998. Tomographic Evidence for Localized Lithospheric Shear along the Altyn Tagh Fault. Science 282, 74–76.